

# The imaginary part of the heavy-quark potential from real-time Yang-Mills dynamics

Kirill Boguslavski

*Institute for Theoretical Physics, Technische Universität Wien, 1040 Vienna, Austria*

Babak S. Kasmaei and Michael Strickland

*Department of Physics, Kent State University, Kent, OH 44242, United States*

## Abstract

We extract the imaginary part of the heavy-quark potential using classical-statistical simulations of real-time Yang-Mills dynamics in classical thermal equilibrium. The  $r$ -dependence of the imaginary part of the potential is extracted by measuring the temporal decay of Wilson loops of spatial length  $r$ . We compare our results to continuum expressions obtained using hard thermal loop theory and to semi-analytic lattice perturbation theory calculations using the hard classical loop formalism. We find that, when plotted as a function of  $m_D r$ , where  $m_D$  is the hard classical loop Debye mass, the imaginary part of the heavy-quark potential is independent of the lattice spacing at small  $r$  and agrees well with the semi-analytic hard classical loop result. For large quark-antiquark separations, we quantify the magnitude of the non-perturbative long-range corrections to the imaginary part of the heavy-quark potential. We present our results for a wide range of temperatures, lattice spacings, and lattice volumes. Based on our results, we extract an estimate of the heavy-quark transport coefficient  $\kappa$  from the short-distance behavior of the classical potential and compare our result with  $\kappa$  obtained using hard thermal loops and hard classical loops. This work sets the stage for extracting the imaginary part of the heavy-quark potential in an expanding non-equilibrium Yang Mills plasma.

## I. INTRODUCTION

At extreme energy densities nuclear matter undergoes a phase transition from a state characterized by confined hadrons to a state in which quarks and gluons become the relevant degrees of freedom. Ultrarelativistic heavy-ion collision experiments at the Relativistic Heavy Ion Collider in New York and the Large Hadron Collider at CERN have now collected a wealth of data concerning the properties of the high energy density phase of nuclear matter, which is called the quark-gluon plasma (QGP) [1]. One of the key observables used in measuring the properties of the QGP is the suppression of heavy quark-antiquark bound states such as bottomonium. The suppression observed by experimentalists gives a measurement of the in-medium breakup rate of bottomonium states and allows one to constrain key plasma observables such as the initial central temperature of the QGP generated in heavy-ion collisions, its shear viscosity to entropy density ratio, and the differential rate at which the QGP expands in non-central collisions (see e.g. [2–5]).

Fundamentally, the computation of the survival probability of a given bottomonium state can be cast into the framework of open quantum systems (OQS) in which there is a probe (bottomonium states) and medium (light quarks and gluons). Within the OQS framework, in order to describe the in-medium evolution of bottomonium states one must trace over the medium degrees of freedom and obtain evolution equations for the reduced density matrix of the system [6–19]. In the limit that the medium relaxation time scale and the intrinsic time scale of the probe are much smaller than the probe relaxation time scale, the resulting dynamical equation for the reduced density matrix can be cast into a so-called Lindblad form [20, 21]. A key outcome of such calculations is that the effective heavy-quark potential possesses an imaginary part which can be related to the total in-medium decay width of the states. This imaginary part has been determined using direct quantum field theoretic or effective field theory calculations [10, 12, 22].

There have been computations of the imaginary part of the heavy-quark potential based on high-temperature quantum chromodynamics (QCD) calculations in the hard thermal loop (HTL) limit [22–29], using effective field theory (pNRQCD) [30–33], finite-temperature lattice QCD [34–43], and real-time classical-statistical solutions of Yang-Mills theory in classical thermal equilibrium [44, 45]. In this work we build upon the studies presented in Ref. [44] and present findings that are complementary to Ref. [45]. In Ref. [44] the authors

presented first results for the imaginary part of the heavy-quark potential using classical-statistical Yang-Mills simulations on spatially 3D lattices of size  $12^3$  and  $16^3$ . In this paper we extend these results to larger lattices up to  $252^3$  and consider SU(2) and SU(3) gauge theories. Additionally, the results of Ref. [44] were presented only for a few spatial points  $r$  in a table. Due to the use of rather large lattice sizes, we can now compute the imaginary part of the heavy quark potential at larger values of  $r/a$  and reconstruct the functional form of the imaginary part of the heavy-quark potential for a much wider range of distances. This allows us to make more precise comparisons between our lattice-extracted imaginary part and (a) results obtained in the continuum limit using hard thermal loops [22] and (b) results obtained using the lattice-regularized hard-classical-loop (HCL) theory [44].

Herein we will present results for the imaginary part of the heavy-quark potential obtained using classical Yang Mills (CYM) simulations of a thermalized gluonic plasma. The use of CYM simulations is motivated by the fact that in situations where (a) gluonic occupation numbers are large, such as in thermal equilibrium for sufficiently low momenta or in the initial stages of heavy-ion collisions, and (b) the gauge coupling is weak  $g^2 \ll 1$ , vacuum contributions to observables are suppressed by powers of the gauge coupling. As a consequence, neglecting vacuum contributions in such cases often leads to a good approximation to the full quantum dynamics.

In order to extract information about thermal systems using CYM, one must prepare the thermalized field configurations. Historically, this is done by preparing 3+1D configurations using Monte-Carlo techniques [46–51]. Herein we follow a simpler strategy and initialize the system close to thermal equilibrium using momentum-space initialization and let the fields thermalize in real time before extracting observables. The advantage of this procedure is that we can run simulations on very large lattices with small lattice spacings  $a$  at moderate computational cost. In practice, however, this means that we have to extract the temperature  $g^2T$  numerically in the thermalized system from correlation functions. We find that this only introduces a small uncertainty for  $g^2T$  of the order of a few percent, which justifies this approach.

One additional complication that arises when dealing with CYM treatments is that they formally do not possess a finite ultraviolet limit due to the Rayleigh-Jeans divergence [50, 52–56]. For this reason, it is important to identify the correct manner in which to scale results in order to extract relevant physical information. We will use the Debye mass  $m_D$  computed

in the hard-classical-loops framework to demonstrate that, when plotted as a function of  $m_D r$ , the imaginary part of the heavy-quark potential is independent of the lattice spacing at small  $r$ . Additionally we find that, when presented in this manner, results obtained using CYM simulations agree well with the semi-analytic hard classical loop result at small quark-antiquark separations. Our study also suggests that the latter approaches a finite form in the continuum limit for all separations. For large quark-antiquark separations, we quantify the magnitude of the non-perturbative long-range corrections to the imaginary part of the heavy-quark potential.

We present our results for a wide range of temperatures, lattice spacings, and lattice volumes, which map to values of  $\beta$  in the range  $16 \rightarrow 300$ . Based on our results, we extract an estimate of the heavy-quark transport coefficient  $\kappa$  and compare our result with  $\kappa$  obtained using hard thermal loops and hard classical loops. This work sets the stage for extracting the out-of-equilibrium imaginary part of the heavy-quark potential in expanding Yang Mills plasmas [57, 58]. Such non-equilibrium extractions are necessary since it is currently unknown how to analytically extract the heavy-quark potential in anisotropic plasmas due the presence of a non-Abelian plasma instability called the chromo-Weibel instability [25, 59–62]. In particular, recent studies have shown that particularly in highly anisotropic systems nonperturbative effects beyond hard loop calculations are crucial [63, 64].

The structure of our paper is as follows. In Sec. II we provide the theoretical background necessary for the computation of the imaginary part of the heavy-quark potential. In Sec. III we present the results from lattice simulations and the comparison of different cases. We present concluding remarks and outlook for future works in Sec. IV.

## II. THEORY AND NUMERICAL SETUP

We consider pure  $SU(N_c)$  gauge theory with the Yang-Mills classical action

$$S[A] = -\frac{1}{2} \int d^4x \text{Tr} (F^{\mu\nu} F_{\mu\nu}), \quad (1)$$

with Einstein sum convention for repeated Lorentz indices  $\mu, \nu = 0, \dots, 3$ . The field strength tensor is given by  $F_{\mu\nu} = \partial_\mu A_\nu - \partial_\nu A_\mu - ig[A_\mu, A_\nu]$  with gauge coupling  $g$ , gauge field  $A_\mu(x)$  and commutator  $[\cdot, \cdot]$ . Unless stated otherwise, we will use  $N_c = 3$ .

## A. Lattice discretization and equations of motion

We use a standard real-time lattice discretization approach where fields are discretized on cubic lattices with  $N^3$  sites and lattice spacing  $a$  (see, e.g., Refs. [58, 65] and references therein for more details). In this real-time approach, spatial gauge fields are replaced by gauge links  $U_j(t, \mathbf{x}) \approx \exp(igaA_j(t, \mathbf{x}))$  at discrete coordinates  $x_k = n_k a$  for  $n_k = 0, \dots, N - 1$ , while temporal gauge with  $A_0 = 0$ , and thus  $U_0 = 1$  is used. The classical equations of motion are written in a gauge-covariant manner as

$$\begin{aligned} U_j(t + a_t/2, \mathbf{x}) &= \exp(ia_t a g E^j(t, \mathbf{x})) U_j(t - a_t/2, \mathbf{x}), \\ g E^j(t + a_t, \mathbf{x}) &= g E^j(t, \mathbf{x}) - \frac{a_t}{a^3} \sum_{j \neq i} [U_{ij}(t - a_t/2, \mathbf{x}) + U_{i(-j)}(t - a_t/2, \mathbf{x})]_{\text{ah}}, \end{aligned} \quad (2)$$

and are solved alternately in a leapfrog scheme [66]. The plaquette is defined as  $U_{ij}(\mathbf{x}) = U_i(\mathbf{x})U_j(\mathbf{x} + \mathbf{a}_i)U_i^\dagger(\mathbf{x} + \mathbf{a}_j)U_i^\dagger(\mathbf{x})$ , and analogously for  $U_{i(-j)}$ , with vectors  $\mathbf{a}_{i/j}$  of length  $a$  in spatial directions  $i, j = 1, 2, 3$ .  $[V]_{\text{ah}} \equiv -i(V - V^\dagger - \text{Tr}(V - V^\dagger)/N_c)/2$  defines the anti-Hermitian traceless part of the matrix  $V$ . The time step is taken to be small, typically  $a_t/a = 0.01$  in this work, to reduce temporal lattice artifacts. The classical equations (2) guarantee that the degree of Gauss law violation is conserved at every time step

$$\begin{aligned} D_j E^j(t, \mathbf{x}) &\equiv \frac{1}{a} \sum_j \left( E^j(t, \mathbf{x}) - U_j^\dagger(t - a_t/2, \mathbf{x} - \mathbf{a}_j) E^j(t, \mathbf{x} - \mathbf{a}_j) U_j(t - a_t/2, \mathbf{x} - \mathbf{a}_j) \right) \\ &= \text{constant}. \end{aligned} \quad (3)$$

Moreover, this lattice discretization guarantees gauge invariance of observables like Wilson loops that are supposed to be gauge invariant.

## B. Computation of observables

Classical observables are computed by averaging over different configurations evolved independently

$$\langle O \rangle(t) \equiv \frac{1}{n} \sum_{j=1}^n O_j(t), \quad (4)$$

and their uncertainty corresponds accordingly to the uncertainty of the mean.

### C. Imaginary part of the classical potential

We are interested in extracting the imaginary part of the classical potential  $V_{\text{cl}}(t, r)$  with  $r \equiv |\mathbf{x}|$ . Following Refs. [22, 44], it can be calculated using

$$i\partial_t C_{\text{cl}}(t, r) = V_{\text{cl}}(t, r)C_{\text{cl}}(t, r), \quad (5)$$

as the asymptotic temporal slope of  $\log[C_{\text{cl}}(t, r)]$ . The classical thermal Wilson loop  $C_{\text{cl}}(t, r)$  is defined as

$$C_{\text{cl}}(t, r) \equiv \frac{1}{N_c} \text{Tr} \langle W[(t_0, \mathbf{x}); (t, \mathbf{x})] W[(t, \mathbf{x}); (t, \mathbf{0})] W[(t, \mathbf{0}); (t_0, \mathbf{0})] W[(t_0, \mathbf{0}); (t_0, \mathbf{x})] \rangle, \quad (6)$$

with temporal Wilson lines  $W[(t_0, \mathbf{x}); (t, \mathbf{x})] = \mathbb{1}$  and spatial Wilson lines  $W[(t, \mathbf{0}); (t, \mathbf{x})] = U_j(t, \mathbf{0})U_j(t, \mathbf{a}_j)U_j(t, 2\mathbf{a}_j) \cdots U_j(t, \mathbf{x})$  for  $\mathbf{x} = \hat{\mathbf{a}}_j r$  and  $\hat{\mathbf{a}}_j = \mathbf{a}_j/a$  being a spatial unit vector. Since the classical thermal state is homogeneous, the Wilson loop is additionally averaged over all lattice points by averaging over the reference coordinates  $\mathbf{0}$ .

In order to extract the imaginary part of  $V_{\text{cl}}(t, r)$  we compute the time-dependence of  $C_{\text{cl}}(t, r)$ . Due to the imaginary part of the in-medium heavy quark potential, this quantity will decay exponentially at late times with the rate of exponential decay set by the imaginary part of  $V_{\text{cl}}(t, r)$ . As a result,  $V_{\text{cl}}(t, r)$  can be computed using the logarithmic slope of this decay as mentioned above. We note that this is formally applicable only in the large- $t$  limit, but we find that an exponential decay is established rather quickly, particularly when using large lattice sizes. We then define the imaginary part of the static classical potential as the late-time limit

$$\text{Im}[V_{\text{cl}}(r)] \equiv \lim_{t \rightarrow \infty} \text{Im}[V_{\text{cl}}(t, r)]. \quad (7)$$

In practice, this agrees with the logarithmic slope extracted from  $C_{\text{cl}}(t, r)$ .

#### D. Construction of quasi-thermalized and fully-thermalized classical states

In order to associate our measurements of  $V_{\text{cl}}(t, r)$  with a specific temperature  $T$ , it is necessary to have a method for self-consistently determining the temperature of the CYM fields. One can construct thermalized CYM configurations using 3+1D Monte-Carlo techniques [46–51]. However, as mentioned in the introduction, we use a simpler technique, which amounts to initializing the fields in a quasi-thermal configuration in momentum-space, as will be explained around (10), and then allowing them to self-thermalize dynamically. On large lattices this method is quite efficient and one finds that the fields self-thermalize quickly. One complication is that the resulting equilibrated temperature  $T$  is different than the quasi-thermal initial temperature  $T_0$  used to initialize the fields in momentum-space. As a result, one must have a method to extract the time-dependent temperature in order to (a) determine when field thermalization is functionally complete and (b) extract the final thermalized temperature of the CYM fields. Once the system is fully thermalized (within an acceptable uncertainty), one can then proceed with the measurement of  $V_{\text{cl}}(t, r)$ .

For this purpose, we extract chromo-electric field correlation functions in Fourier space. In practice, the chromo-electric fields are Fourier transformed as

$$E^j(t, \mathbf{p}) = a^3 \sum_{\mathbf{x}} e^{-2\pi i \sum_k n_k m_k / N} E^j(t, \mathbf{x}), \quad (8)$$

and projected onto normalized transverse vectors  $v_j^\lambda(\mathbf{p})$  with two polarizations  $\lambda = 1, 2$  transverse to the longitudinal polarization vector  $v_j^3(\mathbf{p}) = p_j/p$ , providing  $E_\lambda(t, \mathbf{p})$ . Here we used  $x_k = n_k a$  with  $k = 1, 2, 3$ , the lattice momentum definition  $p_k a = -i(1 - \exp(-2\pi i m_k / N))$ ,  $p^2 = \sum_k |p_k|^2$ , and  $n_k, m_k = 1, \dots, N$ . The correlation functions are then computed as

$$\begin{aligned} \langle EE \rangle_T(t, p) &= \frac{1}{2(Na)^3(N_c^2 - 1)} \sum_{\lambda=1,2} \langle |E_\lambda(t, \mathbf{p})|^2 \rangle \\ \langle EE \rangle_L(t, p) &= \frac{1}{(Na)^3(N_c^2 - 1)} \langle |E_{\lambda=3}(t, \mathbf{p})|^2 \rangle, \end{aligned} \quad (9)$$

and similarly for  $A$  fields. This expression implies averaging over the direction of  $\mathbf{p}$  due to the system's approximate isotropy for not too large momenta and we will consider  $\langle EE \rangle_{T/L}$  as functions of  $p$ .<sup>1</sup> Note that these correlation functions are, in general, gauge dependent. We

<sup>1</sup>Although the anisotropy of the cubic lattice becomes more prominent close to the lattice cutoff at  $|p_k| = 2/a$ ,

get rid of the residual gauge freedom by gauge-fixing to the Coulomb-type gauge  $\partial^j A_j(t, \mathbf{x}) = 0$  to almost machine precision right before computing the correlators.

As mentioned above, while all measurements will be performed in classical thermal equilibrium, for practical purposes we start our simulations in a state very close to thermal equilibrium and let the system dynamically thermalize. We use two-point correlation functions  $\langle EE \rangle$  in Fourier space to check to what extent the system has thermalized. Our procedure is as follows.

We set the fields in Fourier space at initial time  $t = 0$  such that they satisfy

$$\begin{aligned} g^2 \langle EE \rangle_T &= g^2 T_0, & g^2 \langle EE \rangle_L &= 0, \\ g^2 \langle AA \rangle_T &= \frac{g^2 T_0}{p^2}, & g^2 \langle AA \rangle_L &= 0. \end{aligned} \quad (10)$$

These initial conditions can be implemented efficiently by setting (see, e.g., [58, 65, 67])

$$\begin{aligned} gE_a^j(t=0, \mathbf{p}) &= \sqrt{g^2 T_0} \sum_{\lambda=1,2} v_j^\lambda(\mathbf{p}) \beta_a^\lambda(\mathbf{p}) \\ gA_j^a(t=0, \mathbf{p}) &= \sqrt{\frac{g^2 T_0}{p^2}} \sum_{\lambda=1,2} v_j^\lambda(\mathbf{p}) \alpha_a^\lambda(\mathbf{p}), \end{aligned} \quad (11)$$

with the adjoint color index  $a = 1, \dots, N_c^2 - 1$ , and with Gaussian distributed complex random numbers satisfying  $\langle (\alpha_a^\lambda(\mathbf{p}))^* \alpha_b^{\lambda'}(\mathbf{p}') \rangle = \delta_{ab} \delta_{\lambda\lambda'} \delta_{\mathbf{p}\mathbf{p}'} N^3 a^3$ ,  $\langle (\beta_a^\lambda(\mathbf{p}))^* \beta_b^{\lambda'}(\mathbf{p}') \rangle = \delta_{ab} \delta_{\lambda\lambda'} \delta_{\mathbf{p}\mathbf{p}'} N^3 a^3$ , while all other correlations vanish. Subsequently, we restore the Gauss law  $D_j E^j(x) = 0$  with covariant derivative  $D_\mu$  to machine precision using the algorithm in Ref. [49]. This algorithm changes the chromoelectric field correlators mostly at low momenta and, for instance, makes  $\langle EE \rangle_L$  finite. Then we let the system evolve according to the Yang-Mills classical equations of motion (2). Classical thermal equilibrium is reached when the  $\langle EE \rangle_{T/L}(t, p)$  correlation functions do not visibly change over an extended amount of time.

An example of the results obtained using this thermalization algorithm is shown in the left panel of Fig. 1 for  $\langle EE \rangle_T$  and simulation parameters  $g^2 T_0 = 0.375$ ,  $N = 64$ ,  $a = 1$ , averaged over  $N_{\text{config}} = 224$  configurations. The dashed orange horizontal line shows the

---

we will mostly use these correlators as means to extract parameters by fitting to them over a large range of momenta, such that the anisotropic behavior of the cube does not play a significant role here.

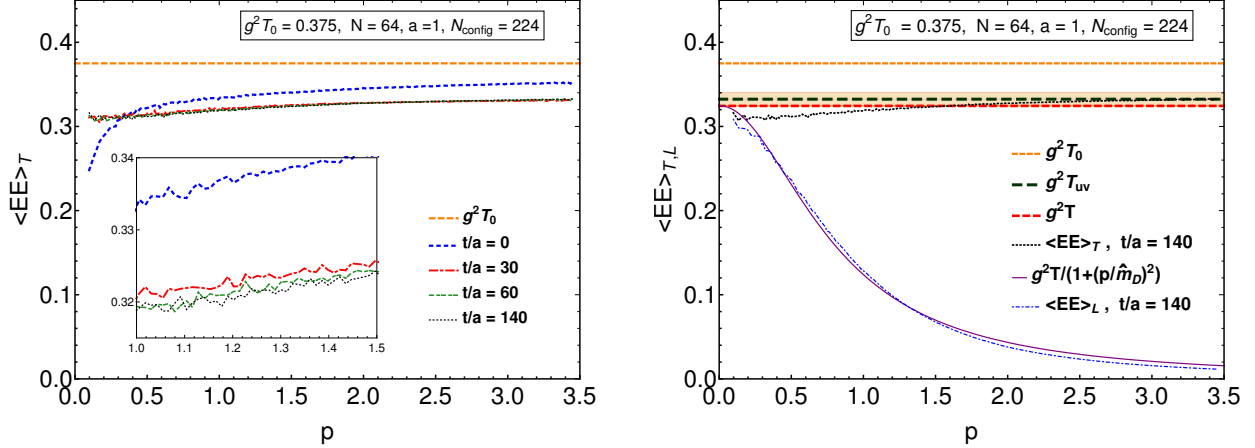


FIG. 1. (Left:) Example of thermalization for  $g^2 T_0 = 3/8$  and  $a = 1$ . The transverse chromo-electric field correlation is shown at different times of the simulated gauge dynamics. The inset shows a zoomed region of the plot. The dashed orange line corresponds to the field initialization (10) with  $g^2 T_0$  before the Gauss law is restored. (Right:) Extracting  $T$  and  $\hat{m}_D$  by fitting (12) to transverse and longitudinal chromo-electric field correlations. The fit functions are given by the black dashed and continuous purple lines. The red dashed line corresponds to the value  $g^2 T_{UV}$  at the hardest momentum, the shaded error band shows the systematic error in the estimation of the temperature  $[T - \Delta T, T + \Delta T]$  with  $\Delta T = T_{UV} - T$ .

initial correlator prior to Gauss law restoration, that equals  $g^2 T_0$  for all momenta. After the restoration, the transverse correlator shows some momentum dependence and is given by the blue dashed line at  $t/a = 0$ . In the subsequent evolution, the system thermalizes rather quickly. Already for times  $t/a \gtrsim 30$ , the correlation function is almost stationary, for later times  $t/a \gtrsim 60$ , the deviation between curves at different times lies within the uncertainty of the data, as can be seen in the inset. At that point, the system can be considered approximately thermal.

As shown in Ref. [68] and recently used in [69], the correlation functions  $\langle EE \rangle_{T/L}(t, p)$  encode the temperature and the Debye mass of the classical state

$$g^2 \langle EE \rangle_T \approx g^2 T, \quad g^2 \langle EE \rangle_L \approx g^2 T \frac{\hat{m}_D^2}{p^2 + \hat{m}_D^2}. \quad (12)$$

These relations are not exact but become more reliable at larger momenta  $p \gg m_D$ . We can use them to extract the temperature  $g^2 T$  and an estimate for the Debye (screening) mass  $\hat{m}_D$ . A systematic error (for  $g^2 T$ ) is estimated as the deviation of the correlators from these simple functional forms, as will be explained shortly. The extraction of these parameters from the transverse and longitudinal chromo-electric field correlations is demonstrated in the right

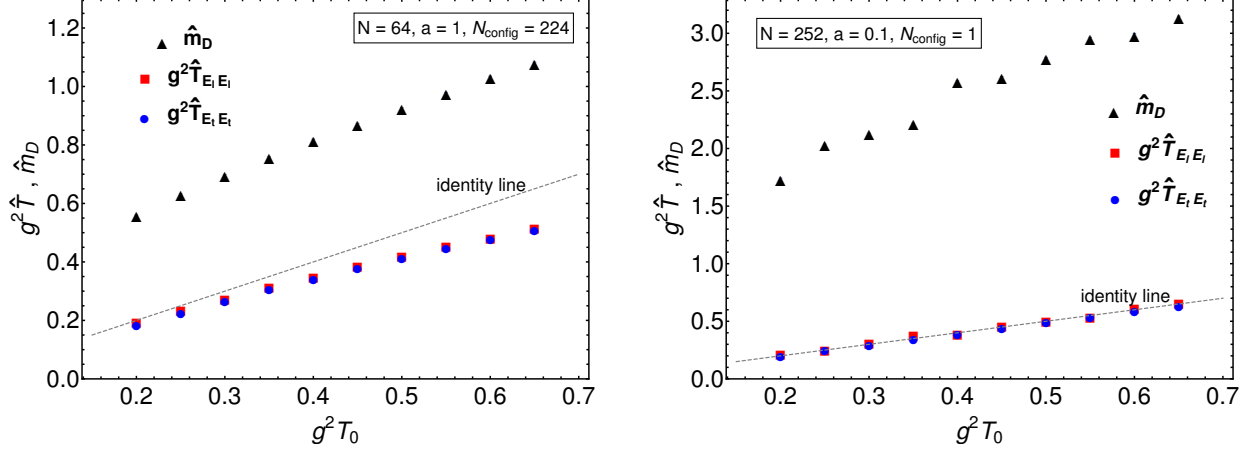


FIG. 2. Extracted values of  $g^2\hat{T}_{E_t E_t}$ ,  $g^2\hat{T}_{E_l E_l}$  and  $\hat{m}_D$  for different values of  $g^2 T_0$  for  $a = 1$  (left) and  $a = 0.1$  (right). All parameters are shown in lattice units.

panel of Fig. 1 for the same parameters as in the left panel at the time  $t/a = 140$ . One can see that the thermalized correlations are lower than the initial value  $g^2 T_0$  for the considered parameters and that they indeed agree well with the fit functions  $g^2\langle EE\rangle_T^{\text{fit}} = g^2\hat{T}_{E_t E_t}$  and  $g^2\langle EE\rangle_L^{\text{fit}} = g^2\hat{T}_{E_l E_l}/(1+p^2/\hat{m}_D^2)$ , as shown by the black dashed and purple continuous lines. Remarkably, these independent fits lead to almost the same value of the temperature and we set

$$g^2 T = g^2\hat{T}_{E_t E_t}. \quad (13)$$

Since the transverse correlator  $\langle EE\rangle_T$  still grows slowly with  $p$ , we extract the value  $g^2 T_{UV}$  at the largest momentum to estimate the error as  $\Delta T = T_{UV} - T$ . This systematic error is shown by the shaded band in the figure. We find that the uncertainty in the extraction of the temperature is generally quite low and becomes smaller with decreasing lattice spacing. For the coarse lattice spacing  $a = 1$  used in Fig. 1, the relative error is only  $\Delta T/T < 3\%$ .

The extracted temperature and mass values,  $g^2\hat{T}_{E_t E_t}$ ,  $g^2\hat{T}_{E_l E_l}$  and  $\hat{m}_D$ , are shown in Fig. 2 as functions of  $g^2 T_0$  for the larger lattice spacing  $a = 1$  (left) and a fine lattice spacing  $a = 0.1$  (right). One observes that both  $g^2\hat{T}_{E_t E_t}$  and  $g^2\hat{T}_{E_l E_l}$ , visible as blue and red points, respectively, agree well in both cases. While for the small lattice spacing,  $g^2 T_0$  and the extracted  $g^2 T$  are almost identical, one observes deviations that grow with temperature for the coarser lattice. Since the lattice simulations depend on the combination  $\beta = 2N_c/(g^2 T a)$ , as will be explained in Sec. II F, we can summarize that deviations increase with decreasing

$\beta$ , while for growing  $\beta$  values, both  $\Delta T/T$  and  $|T_0 - T|/T$  become smaller, enabling a better control of the value of the temperature.

### E. The HTL, HCL, and lattice Debye masses

We will also need to compute the Debye mass in order to compare results obtained using different analytic and numerical approaches. The definition of the Debye mass depends on the method being used. In this paper we consider three methods for defining the Debye mass: (1) continuum hard-thermal-loops calculations, (2) lattice-discretized hard classical loops calculations, and (3) direct lattice measurement using chromo-electric field correlators. The definitions in these three cases are:

1. The well-known continuum hard thermal loop (HTL) expression is

$$m_{D,\text{HTL}}^2 = 4g^2 N_c \int \frac{d^3p}{(2\pi)^3} \frac{f_{\text{BE}}(p)}{p} = \frac{N_c g^2 T}{3}, \quad (14)$$

with the Bose-Einstein distribution  $f_{\text{BE}}(p) = (\exp(p/T) - 1)^{-1}$ .

2. In classical thermal equilibrium one has  $f_{\text{BE}}(p) \rightarrow T/p$ , and the discretization on an anisotropic cubic lattice with a finite lattice spacing leads to the following hard classical loop (HCL) expression

$$m_{D,\text{HCL}}^2 = \frac{g^2 T N_c}{2a} \left( \frac{3\Sigma}{2\pi} - 1 \right), \quad (15)$$

where  $\Sigma \approx 3.1759$  is a factor that results from the anisotropy of the lattice [50]. Strictly speaking, this expression is the leading-order perturbative result in the infinite volume limit. Since we employ large lattice sizes, the latter effect can be neglected. Moreover, finite volume effects are expected to be less important than sub-leading perturbative effects that typically contribute to (14) and (15) at low momenta  $p \lesssim m_D$ . We will use (15) in our figures when we plot the CYM lattice results as a function of  $m_D r$ .

3. Our final possibility is to measure the Debye mass  $\hat{m}_D$  directly from our thermalized CYM configurations using chromo-electric field correlators, which is explained in the previous subsection. Its temperature, and thus  $\beta$  dependence is shown in Fig. 2 for

different lattice spacings. One generally finds that it grows with temperature. More precisely, we find an approximately linear connection to  $m_{D,\text{HCL}}$  with

$$\hat{m}_D \approx 1.42 m_{D,\text{HCL}} \quad (16)$$

for  $92 \leq \beta \leq 300$ , while at lower  $\beta$  deviations from a linear connection become more sizable.

### F. Parameters and scaling properties with the coupling

The coupling  $g$  can be scaled out of the dynamical equations of motion (2) by rescaling all field amplitudes as  $gA \mapsto A$  and  $gE \mapsto E$ . As visible in (12), the coupling then only enters in the combination  $g^2T$ . This dimensionful scale can then be used to make all quantities dimensionless by rescaling them with appropriate powers. In the rescaled version, one then has  $\langle EE \rangle_T \mapsto 1$ . Note that this rescaling implies that lattice simulations only depend on the lattice size  $N^3$  and on the lattice spacings  $g^2Ta \equiv 2N_c/\beta$  and  $g^2Ta_t$ . Since we use  $a_t \ll a$ , temporal artefacts that may result from a dependence on  $g^2Ta_t$  are suppressed, and the simulations mainly depend on

$$\beta = \frac{2N_c}{g^2Ta}. \quad (17)$$

If not stated otherwise, we will write our values for  $a$ ,  $g^2T_0$ , the extracted temperature  $g^2T$  and all dimensionful variables in lattice units. We will also provide the corresponding  $\beta$  values.

## III. RESULTS

In this section we present the non-perturbative results from classical-statistical simulations of real-time Yang-Mills theory on cubic lattices with  $N^3$  sites and the spacing length of  $a$ . As detailed in Sec. II, the fields are initialized with initial temperature  $T_0$ , they thermalize by solving classical equations of motion, and the actual temperature  $T$  is extracted with an error estimate from correlation functions of chromo-electric fields. We present the values of the imaginary part of the classical potential  $\text{Im}[V_{\text{cl}}(r)]$  for  $SU(3)$  extracted from

the evolution of temporal Wilson loops [22, 44]. For comparison, we start this section by recalling the corresponding analytic results from dimensionally regularized HTL and the expressions from lattice-regularized HCL calculations of  $\text{Im}[V_{\text{cl}}(r)]$  to the second-order. We compute the HCL potential numerically for a wide range of  $\beta$  values and fit the numerical HCL results to the functional form of a suitable analytically available approximation with only two parameters. The fit allows us to extract the  $\beta$  dependence of the parameters of the HCL potential, including an estimate for the continuum limit  $\beta \rightarrow \infty$ . We then discuss our numerical results from classical Yang-Mills simulations for a wide range of  $\beta$  values, and compare them with previously published data of  $\text{Im}[V_{\text{cl}}(r)]$  obtained from lattice calculations, with simulations in  $SU(2)$  theory and with HCL results. Finally, we relate the extracted classical potential to the heavy-quark diffusion coefficient  $\kappa$ . Our main simulation results are also summarized in tables in App. A.

### A. Hard Thermal Loop result

In Ref. [22] the authors derived an expression for the imaginary part of the heavy-quark potential to leading-order in the strong coupling constant using the continuum hard thermal loop framework and dimensional regularization. Their final result could be expressed compactly as

$$\text{Im}[V^{(2)}(r)] = -\frac{C_F g^2 T}{4\pi} \phi(m_{D,\text{HTL}} r). \quad (18)$$

where  $C_F = (N_c^2 - 1)/2N_c$ ,

$$\phi(x) \equiv 2 \int_0^\infty dz \frac{z}{(1+z^2)^2} \left[ 1 - \frac{\sin(zx)}{zx} \right], \quad (19)$$

and  $m_{D,\text{HTL}}$  given by the continuum hard thermal loop Debye mass (14). Note that in the large- $r$  limit one has  $\lim_{r \rightarrow \infty} \phi(r) = 1$ . As a result the asymptotic value of the imaginary part in this case is  $-C_F g^2 T/4\pi$ .

### B. Hard Classical Loop results

The result for the imaginary part of the classical potential at infinite volume and infinite time limit ( $N \rightarrow \infty$ ,  $t \rightarrow \infty$ ) from the second-order perturbation theory regularized on a

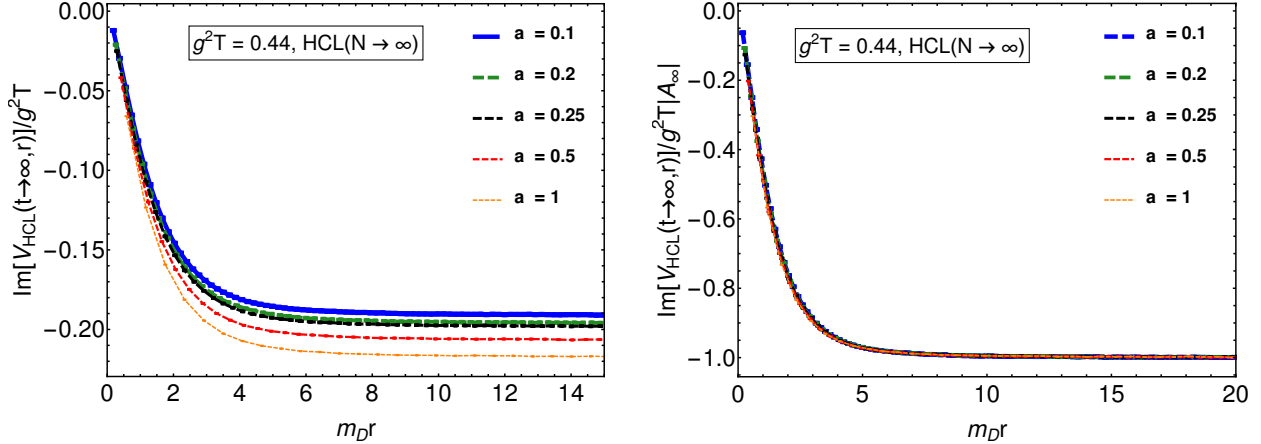


FIG. 3. (Left) Large-time limit of  $\text{Im}[V_{\text{cl}}^{(2)}(r)]/g^2T$  for  $g^2T = 0.44$  and  $a \in \{1, 0.5, 0.25, 0.2, 0.1\}$  corresponding to  $\beta \in \{13.6, 27.3, 54.6, 68.2, 136.4\}$ , calculated using the infinite-volume hard classical loop (HCL) approximation in (20). These numerical results are represented by points while fits using the function (22) are shown as lines. (Right) Same as in the left panel, but divided by the asymptotic value  $A_\infty \equiv \lim_{r \rightarrow \infty} \text{Im}[V_{\text{cl}}^{(2)}(r)]/g^2T$ .

cubic lattice (HCL: Hard Classical Loop) of size  $(aN)^3$  is calculated in Ref. [44] and is given by

$$\text{Im}[V_{\text{cl}}^{(2)}(r)]/g^2T = -\frac{\pi C_F N_c^2}{\beta} \int_0^1 d^3\mathbf{x} \frac{1 - \cos(\pi x_3 r/a)}{(\tilde{\mathbf{x}}^2 + N_c^2 \Sigma / \pi \beta)^2} \int_{-1}^1 d^3\mathbf{y} \frac{\delta(\tilde{\mathbf{x}} \cdot \hat{\mathbf{y}})}{(\hat{\mathbf{y}}^2)^{1/2}}, \quad (20)$$

where the accented variables are defined as

$$\tilde{x}_i \equiv 2 \sin\left(\frac{\pi x_i}{2}\right), \quad \hat{x}_i \equiv \sin(\pi x_i), \quad x_i \in (-1, 1). \quad (21)$$

We perform the numerical integration necessary in (20) using the VEGAS algorithm [70], as implemented in the CUBA library [71]. The results for  $g^2T = 0.44$  and  $a \in \{1, 0.5, 0.25, 0.2, 0.1\}$  corresponding to  $\beta \in \{13.6, 27.3, 54.6, 68.2, 136.4\}$  are shown as points in the left panel of Fig. 3 as functions of  $m_D r$  with  $m_D$  given by the HCL Debye mass (15). As can be seen from this panel, the asymptotic large- $r$  value of  $\text{Im}[V_{\text{HCL}}]$  depends on  $\beta$ , however, the small- $r$  behavior is similar for all values of  $\beta$  shown. We find that the numerical HCL curves are fit very well by the functional form

$$\text{Im}[V_{\text{cl}}^{(2)}(r)] = g^2T A_\infty \phi(B m_D r). \quad (22)$$

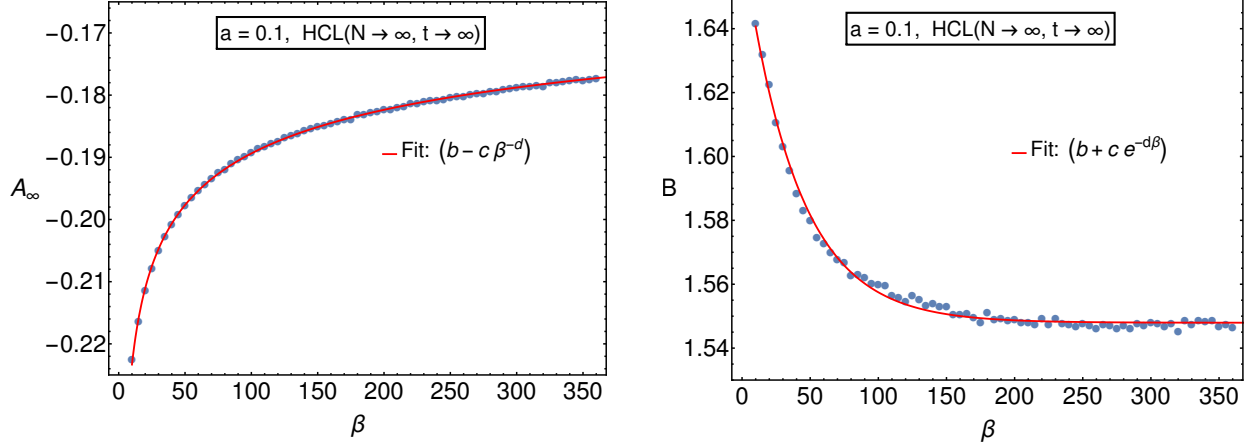


FIG. 4. Fit values  $A_\infty^{\text{HCL}}$  (left) and  $B^{\text{HCL}}$  (right) of the fit function (22) to the classical potential  $\text{Im}[V_{\text{cl}}^{(2)}(r)]/g^2T$  computed within HCL for a wide parameter range  $\beta = 10 \rightarrow 360$  for  $a = 0.1$ . Fits to the dependence of these parameters on  $\beta$  are shown as red curves, with the chosen form of the fit functions indicated in the label. The asymptotic values are  $A_\infty^{\text{HCL}}(\beta \rightarrow \infty) = -0.144$  and  $B^{\text{HCL}}(\beta \rightarrow \infty) = 1.55$ .

with  $\phi(x)$  given in Eq. (19). This functional form is motivated by the analytic leading-order perturbative HTL result (18) for which  $A_\infty^{\text{HTL}} = -C_F/4\pi$  and  $B^{\text{HTL}} = 1$  with the HTL calculated  $m_D$ . The fitted curves are shown as lines in Fig. 3 and nicely coincide with the numerically integrated results.

To make the agreement better visible, we show in the right panel of Fig. 3 the same results divided by their corresponding asymptotic values  $A_\infty^{\text{HCL}}$ . All curves fall on top of each other, demonstrating that  $\text{Im}[V_{\text{cl}}^{(2)}(r)]/(g^2T A_\infty^{\text{HCL}})$  is well described by  $\phi(B^{\text{HCL}} m_{D,\text{HCL}} r)$ . This also shows that, while fitted values of  $A_\infty^{\text{HCL}}$  depend on  $\beta$ , this functional form and, in particular, the parameter  $B^{\text{HCL}}$  is barely sensitive to  $\beta$  in the considered range of  $\beta$  values.

We show the fitted parameters  $A_\infty^{\text{HCL}}$  and  $B^{\text{HCL}}$  in Fig. 4 for a wide range  $10 \leq \beta \leq 360$ . Consistent to our earlier observations,  $B^{\text{HCL}}$  becomes practically constant at large  $\beta$ , while  $A_\infty^{\text{HCL}}$  is still growing for the values considered here. To better understand the functional form of the parameters and to extrapolate to larger  $\beta$ , we have performed fits with different functional forms. The functions that seem to describe the results in the best way are

$$\begin{aligned}
 A_\infty^{\text{HCL}}(\beta) &\approx -0.144 - 0.139 \beta^{-0.24} \\
 B^{\text{HCL}}(\beta) &\approx 1.548 + 0.12 e^{-0.025\beta},
 \end{aligned}
 \tag{23}$$

and are included into Fig. 4 as red continuous lines.<sup>2</sup> The fit functions allow us to estimate the asymptotic values

$$A_{\infty}^{\text{HCL}}(\beta \rightarrow \infty) \approx -0.144 = -0.108 C_F, \quad B^{\text{HCL}}(\beta \rightarrow \infty) \approx 1.548. \quad (24)$$

Since the large- $\beta$  limit corresponds to the limit  $a \rightarrow 0$ , the existence of such a continuum limit for an observable is very nontrivial in classical thermal lattice field theory due to the Rayleigh-Jeans divergence. Our analysis suggests that such a limit exists for  $\text{Im}[V_{\text{cl}}^{(2)}(r)]$ . This was possible in our case because, different from previous studies, we studied the HCL potential as a function of  $m_{D,\text{HCL}} r$  rather than any other combination of the lattice spacing or the temperature. Since  $m_{D,\text{HCL}}$  diverges for small  $a$ , our parametrisation hides the divergence and leaves the functional form and the remaining parameters finite. It is interesting to compare the extrapolated parameter values (24) to the corresponding HTL values in dimensional regularization of Sec. III A. As mentioned before, these are

$$A_{\infty}^{\text{HTL}} \approx -0.08 C_F, \quad B^{\text{HTL}} = 1. \quad (25)$$

The  $A_{\infty}$  values are quite close, with the estimated HCL value  $|A_{\infty}^{\text{HCL}}(\beta \rightarrow \infty)|$  being 35% larger than the corresponding HTL value. Note here that our extrapolation is expected to have a large uncertainty for  $A_{\infty}^{\text{HCL}}$  for  $\beta \rightarrow \infty$  since its value is still quite rapidly changing in the considered  $\beta$  interval, as seen in Fig. 4. While the fit works surprisingly well over a large  $\beta$  interval, which gave us confidence to write a limiting value, our analysis is not a proof that  $|A_{\infty}^{\text{HCL}}(\beta \rightarrow \infty)|$  is indeed finite but rather an observation from this fit function. This is different for the parameter  $B$ , that agrees well with its estimated continuum limit for  $\beta \gtrsim 200$ . Since  $B$  multiplies the divergent Debye mass, the product  $B m_{D,\text{HCL}}$  could be interpreted as a suitable adjustment of the lattice regularized mass.

### C. Nonperturbative CYM simulation results for the classical Wilson loop

We now turn to the results of our CYM lattice simulations. To extract the imaginary part of the classical potential  $\text{Im}[V_{\text{cl}}(r)]$  from non-perturbative lattice simulations, we follow

<sup>2</sup>We tried both functional forms for each of the parameters  $A_{\infty}$  and  $B$  and found that these forms shown in the plots are preferred by far.

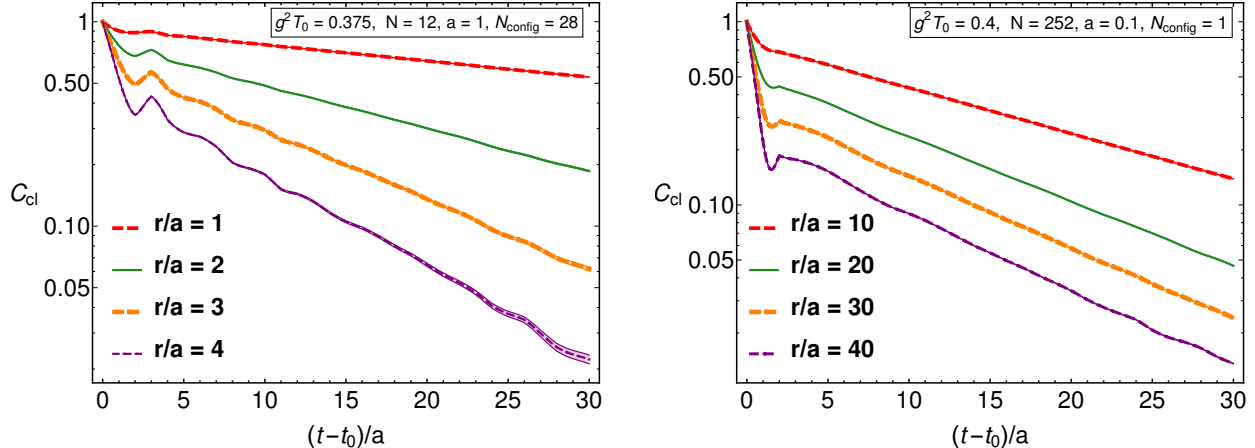


FIG. 5. Examples of the classical Wilson loop as a function of time for lattice spacing  $a = 1$  and spatial separation values  $r/a = \{1, 2, 3, 4\}$  (left), and for lattice spacing  $a = 0.1$  and spatial separation values  $r/a = \{10, 20, 30, 40\}$  (right).

the procedure introduced in Ref. [44] and revisited in Sec. II C. We consider rectangular Wilson loops of different spatial size  $r = na$  and temporal length  $t = n_t a_t$ .<sup>3</sup> We use a temporal lattice spacing of  $a_t = a/100$  for all results reported in this paper. The imaginary part of the classical potential  $\text{Im}[V_{\text{cl}}(r)]$  at separation  $r$  for a heavy quarkonium system is calculated from the large-time slope of the logarithm of the Wilson loop  $C_{\text{cl}}(r, t)$ , averaged over lattice sites, orientations and configurations. The time evolution of  $C_{\text{cl}}(r, t)$  is shown for two example cases in Fig. 5.

In the left panel of Fig. 5 we present typical results obtained on a small lattice which is averaged over  $N_{\text{config}} = 28$  classical-statistical configurations. The bands indicate the uncertainty in the mean obtained by dividing the standard deviation from the mean value by  $\sqrt{N_{\text{config}} N_{\text{iso}} N_{\text{start.points}}}$ . As indicated from this last expression, we exploit the isotropy and homogeneity of the lattice in order to obtain increased statistics, where we average over two different Wilson loop orientations and use  $N_{\text{start.points}} = N^3$  possible spatial starting points from which we can measure the Wilson loop. As can be seen from this panel, one cannot perform the fits to extract the logarithmic slope at early times. In practice, one must wait a sufficient amount of time beyond the thermalization time ( $t_0$ ). Typically, we use a fit window that encompasses  $(t - t_0)/a > 10$ . We find that as long as one uses starting times for the fit window which satisfy this constraint, there is only a very small variation in the extracted logarithmic slopes.

<sup>3</sup>Since we work in temporal axial gauge with  $U_0 = 1$ , the temporal edges of the Wilson loops are trivial and the loops reduce to line-line correlators.

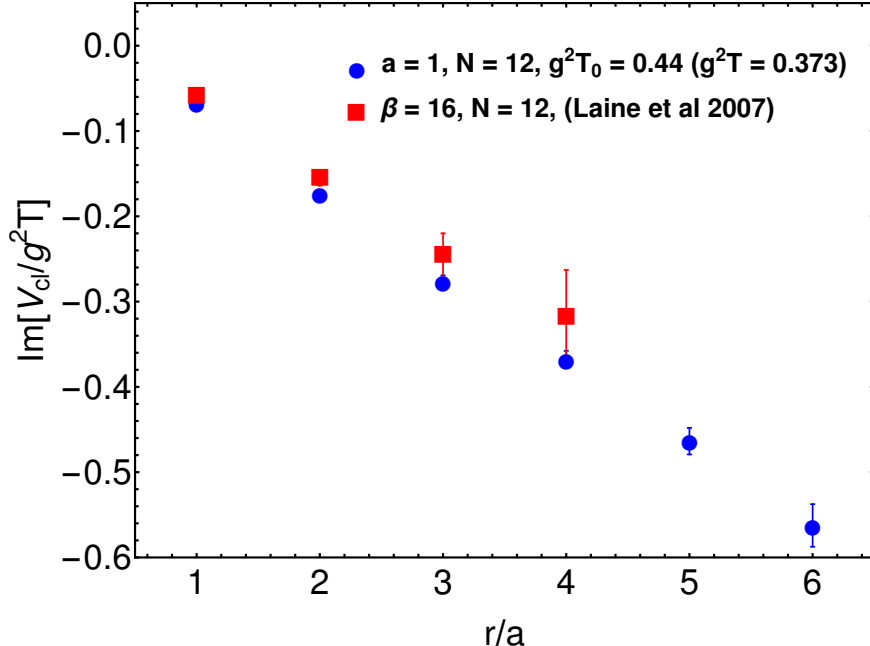


FIG. 6.  $\text{Im}[V_{\text{cl}}(r)]/g^2T$  as a function of  $r/a$  for  $\beta = 16$ . The blue filled disks are the results obtained herein averaged over 28 configurations. The red filled squares are the results reported by Laine et al. in Ref. [44].

In the right panel of Fig. 5 we present typical results obtained on a large lattice in which we only take into account one configuration for the initial fields. As this panel demonstrates, when using large lattices, the uncertainty is decreased due to the much larger number of starting points that can be used to measure the Wilson loop. As a result, on large lattices one does not need to sample as many initial configurations, which helps to reduce the run time required to extract statistically accurate results. We have explicitly checked that the uncertainty bands obtained with one initial configuration are consistent with results obtained using larger number of initial configurations but a smaller lattice size.

#### 1. Benchmark results for $\beta = 16$ and $a = 1$

In Fig. 6 we compare our results to the previously available ones from Ref. [44] for  $\beta = 16$ . We set the parameter  $g^2T_0 = 0.44$  for the initial distribution so that the resulting temperature extracted from  $\langle EE \rangle$  correlators is  $g^2T \approx 0.373$ , which is close to the value  $g^2T = 0.375$  for the corresponding  $\beta = 16$  when setting  $a = 1$ ,  $g^2 = 1$ . The error bars indicated in Fig. 6 include uncertainties from averaging the Wilson loops over the starting points, orientations, classical configurations, uncertainties coming from the fitting residuals,

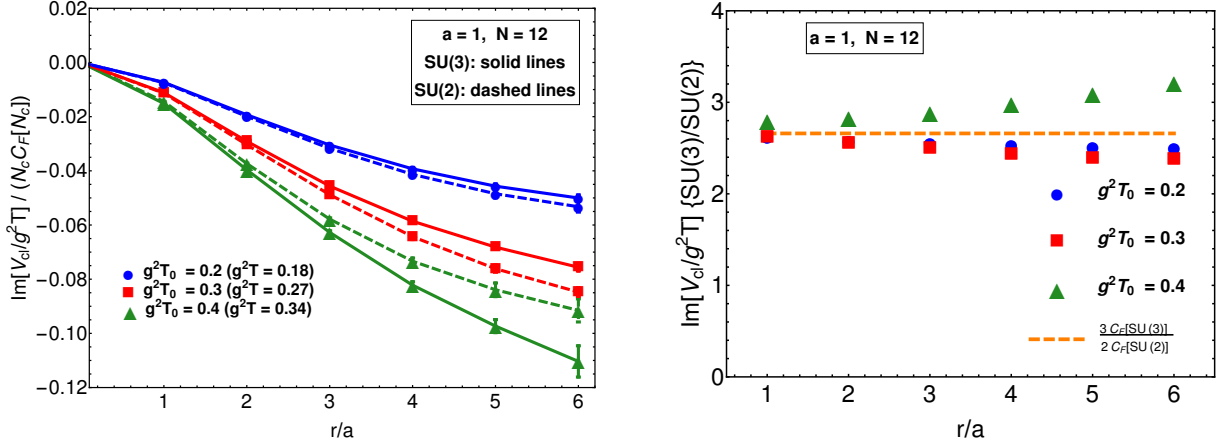


FIG. 7. *Left:*  $\text{Im}[V_{\text{cl}}(r)]/g^2 T$  extracted from  $SU(2)$  and  $SU(3)$  lattice gauge theories simulated with the same values  $T_0$ . The given values of  $T$  correspond to  $SU(3)$ . The potential is divided by  $C_F N_c$  of the respective gauge group. *Right:* The ratios of  $SU(3)$  to  $SU(2)$  results for  $\text{Im}[V_{\text{cl}}(r)]/g^2 T$  for the same simulations. The orange dashed line corresponds to  $8/3$ .

and uncertainties from the temperature extraction. As can be seen from this Figure, our results are in agreement within uncertainties with the reported results from Ref. [44].

## 2. Comparing results for $SU(3)$ vs. $SU(2)$

To check for the  $N_c$  dependence of the  $SU(N_c)$  gauge theories, we perform here similar lattice calculations for  $SU(3)$  and  $SU(2)$  systems and extract  $\text{Im}[V_{\text{cl}}(r)]/g^2 T$  for different values of  $T_0$ . In Fig. 7 we use the same lattice parameters  $a = 1$  and  $N = 12$  as we did in Fig. 6 and compare the simulations for the values  $g^2 T_0 = \{0.2, 0.3, 0.4\}$ . In the left panel of Fig. 7, the values of the ratio  $\text{Im}[V_{\text{cl}}(r)]/(g^2 T C_F N_c)$  are shown for the two gauge groups as functions of  $r/a$ . One finds that they agree well at low  $r/a$  while the deviations grow with the distance. However, the agreement improves for smaller temperatures (larger  $\beta$  values).

In the right panel, the ratio of the imaginary parts of the potentials of the  $SU(3)$  and  $SU(2)$  theories,  $(\text{Im}[V_{\text{cl}}(r)]/(g^2 T)[SU(3)]) / (\text{Im}[V_{\text{cl}}(r)]/(g^2 T)[SU(2)])$ , is plotted as a function of  $r/a$ . The horizontal dashed line corresponds to  $(N_c C_F [SU(3)]) / (N_c C_F [SU(2)]) = 8/3$ , which is the ratio of their  $N_c C_F$  values. One observes that the data points are close to this value for all  $r$  and  $T_0$ , which shows that the imaginary part of the potential in our

lattice simulations admits Casimir scaling

$$\text{Im}[V_{\text{cl}}(r)] \propto C_F N_c. \quad (26)$$

This is similar to the perturbative HCL expression (20) where due to  $\beta \propto N_c$ , one also finds this relation (26).

The deviations visible in the right panel of Fig. 7 decrease with increasing  $\beta$  (smaller temperature) and with decreasing distance, as we have observed in the left panel. An important source for these deviations is that we compare here simulations with the same  $g^2 T_0$  parameter and not with the same temperature  $g^2 T$ . As visible in the left panel of Fig. 2 for  $a = 1$  and  $SU(3)$  theory, the extracted temperatures deviate stronger at larger  $g^2 T_0$ . The deviations in  $SU(2)$  theory are qualitatively similar but can lead to quantitatively different values of  $g^2 T$ , which implies that we compare the  $SU(N_c)$  theories effectively at slightly different temperatures. This effect is reduced when going to smaller temperatures or smaller lattice spacings (larger  $\beta$  values). Moreover, as we will show below, the short-distance behavior is less sensitive to the temperature, which is the reason why the deviations decrease at lower  $r/a$ .

### 3. $SU(3)$ simulation results for different $\beta$

We performed CYM lattice simulations with  $g^2 T_0 = 0.44$  and  $a = \{1, 0.5, 0.25, 0.2\}$  keeping  $aN = 12$  fixed and also for  $g^2 T_0 = 0.45$  and  $a = 0.1$  with  $N = 252$ . Our results for  $\text{Im}[V_{\text{cl}}(r)]/g^2 T$  are shown in Fig. 8 as points connected by solid colored lines, and the respective  $\beta$  values are written in the figure. The  $a = 0.1$  CYM lattice simulation results are compared with the corresponding results (same  $a$  and  $T$ ) obtained from HCL perturbation theory (20), included as a blue dashed curve. For both our CYM lattice results and the HCL results,  $\text{Im}[V_{\text{cl}}(r)]/g^2 T$  is plotted as a function of  $m_D r$ , where we use the leading-order Debye mass  $m_{D,\text{HCL}}$  calculated in HCL theory (15). On the right edge of the figure we indicate the asymptotic  $r \rightarrow \infty$  values obtained using both the dimensionally-regularized continuum HTL result (18) and the extrapolated  $N, \beta \rightarrow \infty$  HCL result with the parameters (24).

As can be seen from this Figure (Fig. 8), the CYM lattice results seem to have a well-defined continuum limit for  $\beta \rightarrow \infty$  when plotted as a function of  $m_D r$ , with the CYM results

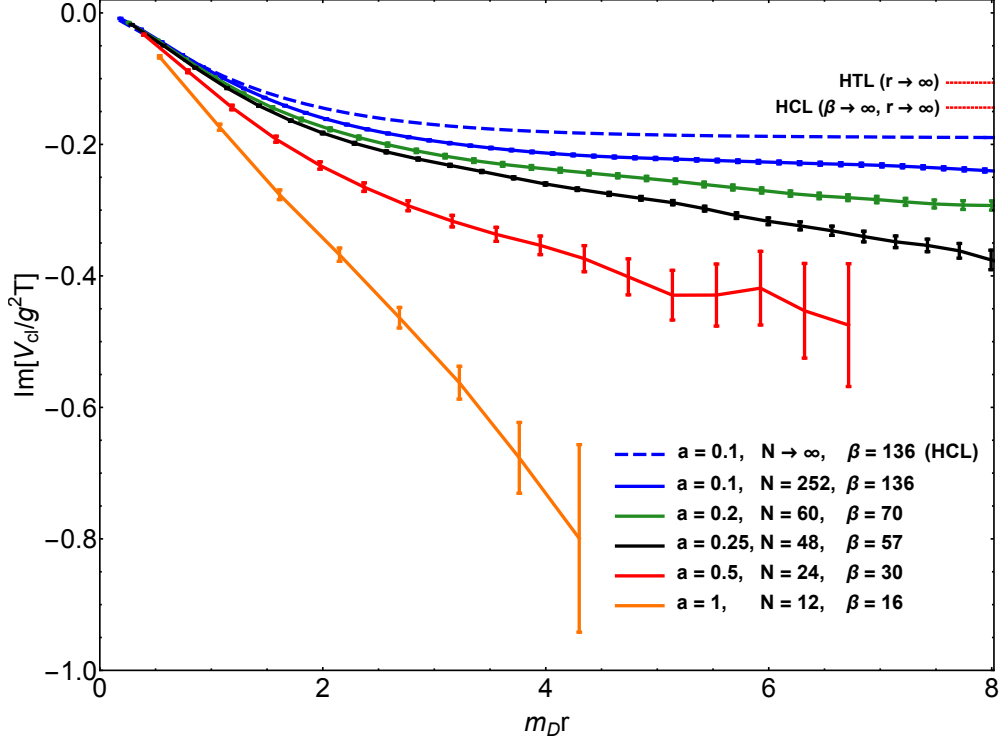


FIG. 8.  $\text{Im}[V_{\text{cl}}(r)]/g^2T$  for different lattice spacing from nonperturbative Wilson loops (solid lines) and from HCL perturbation theory for  $a = 0.1$  (blue dashed line). The temperature values (extracted from  $EE$  correlations) are slightly different for different values of  $a$ , and we write the corresponding  $\beta$  values instead. The  $r \rightarrow \infty$  limits of HCL for the continuum extrapolation  $\beta \rightarrow \infty$  (24) and of the dimensionally-regularized HTL perturbation theories (25) are indicated by short dotted red lines on the right axis for comparison. The distance in the horizontal axis is scaled using the HCL Debye mass (15) for  $m_D(a)$ .

with  $\beta = 136$  overlapping with the corresponding HCL curve at  $m_D r \lesssim 1$ . At large values of  $r$  our CYM simulation results approach the corresponding HCL results for the respective  $\beta$  value. For the largest  $\beta = 136$  in the figure, we know from the left panel of Fig. 4 that the amplitude of the potential at large  $r$  is still quite far away from the extrapolated value. However, Fig. 8 indicates that the CYM potential is approaching the HCL continuum limit from below. The relatively good agreement between our non-perturbative CYM results and the perturbative HCL results at small and large  $r$  indicates that the classical imaginary part of the heavy-quark potential is quite well approximated by the continuum HCL result, and hence is largely, if not entirely, dominated by perturbative physics.

We emphasize that, while previous studies showed the potential for different  $\beta$  values as functions of  $r/a$ , we find that plotting it as a function of  $m_D r$  makes the comparison more intuitive. Most importantly, this allows to extrapolate the potential to large  $\beta$  values

without encountering divergences. We have performed such a continuum extrapolation for the HCL calculations already in Sec. III B by considering  $\text{Im}[V_{\text{cl}}(r)]/g^2T$  as a function of  $m_{D,\text{HCL}} r$  for increasing  $\beta$ . Note that a classical divergence appears in the imaginary part of the potential, however, it is moved into the Debye mass  $m_{D,\text{HCL}}^2 \sim g^2T/a$ , while leaving the functional form of the potential finite.

Instead of the leading-order perturbative HCL mass  $m_{D,\text{HCL}}$ , one could instead plot the CYM results as a function of  $\hat{m}_D r$ , with the values of  $\hat{m}_D$  extracted from CYM longitudinal chromoelectric field correlators as discussed in Sec. II D. The latter is an estimate of the Debye mass including higher-order and nonperturbative contributions. We find that, in practice, the HCL Debye mass (20) is proportional to the correlator-extracted Debye mass  $\hat{m}_D$  over a wide range of  $\beta$  via Eq. (16) with proportionality constant 1.42, and that the resulting rescaling only introduces a constant rescaling of the horizontal axis. Since there are larger uncertainties inherent in the extraction of  $\hat{m}_D$  from the chromoelectric correlators, we have chosen to rescale the classical lattice and HCL results using the same HCL mass definition.

#### D. Relation to heavy-quark diffusion coefficient

The heavy-quark diffusion coefficient  $\kappa$  measures the momentum broadening of a heavy quark due to interactions with the plasma

$$\frac{d}{dt}\langle(\Delta p)^2\rangle = \kappa. \quad (27)$$

Defining it in terms of an unequal-time correlation function of chromo-electric fields  $E$ , with temporal Wilson lines in the definition to make it gauge invariant, it has been computed analytically in perturbation theory up to next-to-leading order [72–74] and numerically using standard lattice QCD [75–81] and lattice QCD in classical thermal equilibrium [82]. The heavy-quark diffusion coefficient has also recently been computed for an over-occupied gluonic plasma out of equilibrium using classical-statistical lattice simulations, with the result that  $\kappa$  can be large at initial stages in heavy-ion collisions [83].<sup>4</sup>

Importantly, the heavy-quark diffusion coefficient can be connected to the small-distance

<sup>4</sup>A similar conclusion has been found for the jet quenching parameter  $\hat{q}$  for initial stages of heavy-ion collisions [84, 85].

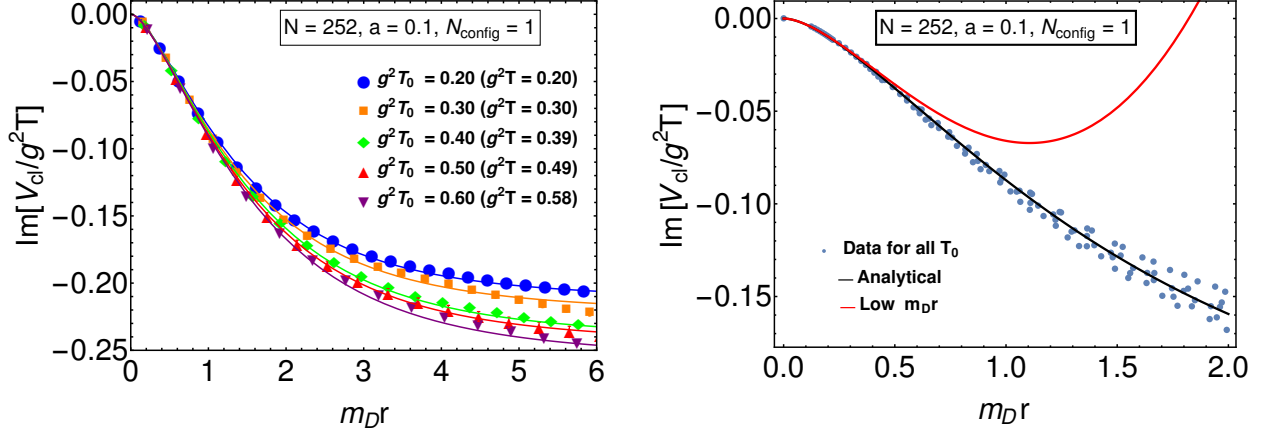


FIG. 9. (Left) The extracted classical potential  $\text{Im}[V_{\text{cl}}(r)]/g^2T$  as a function of  $m_D r$  for fixed lattice spacing  $a = 0.1$  but for different temperatures  $g^2T = 0.2, \dots, 0.59$ , which correspond to the range  $\beta = 300, \dots, 100$ . The continuous curves are fits to our data points using the form of the potential in (22). (Right) The combined data of the left panel, with additional data sets for  $g^2T_0 = 0.25, 0.35, 0.45, 0.55, 0.65$ , is compared to the analytical form (22) with parameter values (30) and its low-distance limit (31) as black and red curves, respectively.

behavior of the imaginary part of the heavy-quark potential. To see this, let us first consider the fitting functional (22) with parameter  $A_\infty$  and  $B$ . We saw previously that the imaginary part of the heavy-quark potential agrees with this form in both the HTL and the HCL formalisms with the parameters

$$A_\infty^{\text{HTL}} \approx -0.080 C_F, \quad B^{\text{HTL}} = 1 \quad (28)$$

$$A_\infty^{\text{HCL}}(\beta \rightarrow \infty) \approx -0.108 C_F, \quad B^{\text{HCL}}(\beta \rightarrow \infty) \approx 1.548. \quad (29)$$

We show here that, at small distances, the classical potential extracted from our lattice simulation data also follows the functional form (22). This is shown in the left panel of Fig. 9, where  $\text{Im}[V_{\text{cl}}(r)]/g^2T$  for fixed lattice spacing  $a = 0.1$  is plotted for different temperatures corresponding to  $100 \lesssim \beta \leq 300$ , as a function of  $m_D r$ . Fits to each data set using (22) in the considered interval  $m_D r \leq 6$  are included as continuous lines. One finds a very good agreement between the data and the respective fits. Moreover, although  $m_D$  and the extracted potential vary with the temperature  $T$  and, equivalently, with  $\beta$ , all curves are seen to fall on top of each other at low distances  $m_D r \lesssim 1$ , marking approximately temperature-independent low-distance behavior for the considered  $\beta$  interval. Averaging

over the resulting parameter values, we obtain

$$A_\infty^{\text{latt}} = -0.24 \pm 0.02 = (-0.18 \pm 0.015) C_F, \quad B^{\text{latt}} = 1.2 \pm 0.05 \quad (30)$$

Here the error has been estimated by the standard deviation and the fitting error.

In the right panel of Fig. 9, we combine all of the curves of the left panel and compare them to the function (22) with the mean parameter values in (30), shown as a black line. One observes a very good agreement with our data, especially at low distances  $m_D r$ . We can now perform a short-distance expansion of the fitting function for the imaginary part of the potential (22), neglecting terms  $\mathcal{O}((m_D r)^4)$ ,

$$\text{Im}[V_{\text{cl}}(r)] \simeq -r^2 \frac{1}{9} |A_\infty| B^2 g^2 T m_D^2 (4 - 3\gamma - 3 \log(B m_D r)), \quad (31)$$

which is shown as a red line and is observed to agree well with our data for  $m_D r \lesssim 0.5$ . For these low distances one finds from (31)

$$\text{Im}[V_{\text{cl}}(r)] \propto A_\infty m_D^2 \propto C_F N_c, \quad (32)$$

which is the Casimir scaling that we observed in Sec. III C 2.

Let us now return to the heavy-quark diffusion coefficient  $\kappa$ . For this, we rewrite the low-distance expression of  $\text{Im}[V_{\text{cl}}(r)]$  in (31) by adding and subtracting constants and terms involving  $\log T$  in the brackets

$$\begin{aligned} & \text{Im}[V_{\text{cl}}(r)] \\ & \simeq -\frac{1}{2} r^2 \left[ \frac{2}{9} |A_\infty| B^2 g^2 T m_D^2 \left( 3 \log\left(\frac{T}{m_D}\right) + 4 - 3\gamma - 3 \log\left(\frac{2B}{D}\right) - 3 \log\left(\frac{DrT}{2}\right) \right) \right]. \end{aligned} \quad (33)$$

Here we have added a parameter  $D \sim \mathcal{O}(1)$  that we will adjust below. For short distances  $r \sim 1/T$ , the last term can be neglected and one obtains

$$\text{Im}[V_{\text{cl}}^{(2)}(r)] \simeq -\frac{1}{2} \kappa_V r^2 \quad (34)$$

with

$$\kappa_V \approx \frac{2}{3} |A_\infty| B^2 g^2 T m_D^2 \left( \log\left(\frac{T}{m_D}\right) + \frac{4}{3} - \gamma - \log\left(\frac{2B}{D}\right) \right), \quad (35)$$

where we added a subscript  $V$  to indicate that this expression is extracted from the classical potential. We can use it to compare to computations of  $\kappa$  with other methods. Let us first consider the continuum HTL result  $\text{Im}[V^{(2)}(r)]$  of (18), which corresponds to the fitting form of the potential (22) with the parameter values (28). Plugging them into (35) leads to the expression

$$\kappa_V^{\text{HTL}} \approx \frac{C_F}{6\pi} g^2 T m_{D,\text{HTL}}^2 \left( \log\left(\frac{T}{m_{D,\text{HTL}}}\right) + \frac{4}{3} - \gamma + \log\left(\frac{D}{2}\right) \right). \quad (36)$$

We can compare this result to direct diagrammatic calculations of the heavy-quark diffusion coefficient in dimensional regularization [72, 73] at leading order

$$\kappa_{\text{dir}}^{\text{HTL}} \approx \frac{C_F}{6\pi} g^2 T m_{D,\text{HTL}}^2 \left( \log\left(\frac{T}{m_{D,\text{HTL}}}\right) + \frac{1}{2} - \gamma + \log 2 + \frac{\zeta'(2)}{\zeta(2)} \right) \quad (37)$$

$$\approx C_F g^2 T m_{D,\text{HTL}}^2 \left( 0.053 \log\left(\frac{T}{m_{D,\text{HTL}}}\right) + 0.0024 \right). \quad (38)$$

The leading logarithmic term is identical in both expressions, verifying that both calculations are consistent. We adjust the residual parameter  $D$  by equating both expressions. This leads to

$$D^{\text{HTL}} = 2 \exp\left(-\frac{5}{6} + \log(2) + \frac{\zeta'(2)}{\zeta(2)}\right) \approx 0.98. \quad (39)$$

Hence, the HTL heavy-quark diffusion coefficient extracted from the heavy-quark potential and the coefficient calculated directly using perturbation theory agree at leading logarithmic accuracy precisely. We have adjusted an additional parameter  $D \approx 1$  to make them agree also at full leading order in the coupling  $g \sim m_D/T$ . This agreement is valid at distances  $r \sim 1/T$ .

With this value  $D = D^{\text{HTL}}$  and the parameter values in Eqs. (30) and (29), we can finally write down our results for the heavy-quark diffusion coefficient from HCL calculations in

the continuum limit  $\beta \rightarrow \infty$  and from classical lattice simulations

$$\begin{aligned}\kappa_V^{\text{HCL}} &\approx C_F g^2 T m_{D,\text{HCL}}^2 \left( 0.173 \log \left( \frac{T}{m_{D,\text{HCL}}} \right) - 0.067 \right) \\ \kappa_V^{\text{latt}} &\approx C_F g^2 T m_{D,\text{HCL}}^2 \left( 0.173 \log \left( \frac{T}{m_{D,\text{HCL}}} \right) - 0.023 \right).\end{aligned}\quad (40)$$

The values of the numerical parameters in these expressions are almost identical although the values for  $A_\infty$  and  $B$  are quite different for our HCL and lattice results. This explains the very good agreement at low distances among the curves displayed in Figs. 8 and 9. However, the leading logarithmic numerical value 0.173 in (40) is larger by a factor of more than 3 than the perturbative HTL result (38).

Since the numerical prefactor of the leading logarithmic term is  $\propto A_\infty B^2$ , the difference between the HCL and HTL values is consistent with the respective difference for  $A_\infty$  and  $B$  in (28) and (29). They mainly deviate in their values for  $B$ , which enters all expressions as a factor of the Debye mass  $m_D$ . It therefore depends on the renormalization of the Debye mass, as we discussed in Sec. III B, and on its definition. In fact, for the lattice simulations we could, for instance, have used the Debye mass  $\hat{m}_D$  instead, which is extracted from the longitudinal correlation function of chromoelectric fields in (12). The resulting heavy-quark diffusion coefficient, expressed with  $\hat{m}_D$  instead of  $m_{D,\text{HCL}}$  as in (40), reads

$$\kappa_V^{\text{latt}} \approx C_F g^2 T \hat{m}_D^2 \left( 0.086 \log \left( \frac{T}{\hat{m}_D} \right) + 0.018 \right).\quad (41)$$

The leading logarithmic numerical prefactor is now much closer to the corresponding HTL value in (38). Regardless of this complication, our calculation of  $\kappa$  in HCL and classical lattice field theory shows the same parametric dependencies on  $C_F$ ,  $g^2$ ,  $T$  and  $m_D$ , as one expects from the HTL result.

In summary, we have observed numerically that the classical potential on the lattice is also given by the analytical form in (22) for sufficiently small quark-antiquark separations. Its low-distance behavior at  $r \sim 1/T$  can be written as  $\text{Im}[V_{\text{cl}}^{(2)}(r)] \simeq -\frac{1}{2} \kappa r^2$  with the heavy quark diffusion coefficient  $\kappa$ . We have shown explicitly for the continuum HTL theory that for such distances, the expression for  $\kappa$  is identical to its direct calculation in continuum perturbation theory. We have found that our extracted values for  $\kappa$  from lattice simulations in classical equilibrium are almost the same as those obtained in HCL theory. Indeed,

they can even get close to the HTL values by using a suitable definition or computation of the Debye mass. Our analysis demonstrates as a proof of concept that one can extract a heavy-quark diffusion coefficient from the classical potential at low distances.

#### IV. CONCLUSIONS AND OUTLOOK

In this paper we used classical-statistical lattice simulations of pure Yang-Mills fields to extract the imaginary part of the heavy-quark potential as a function of the quark-antiquark separation. In order to carry out our simulations on large lattices, we used a simplified scheme to generate thermalized gauge field configurations which relied on initialization of chromoelectric fields in momentum-space followed by a period of self-thermalization. In order to determine whether the fields were thermalized, we extracted the temperature of the system as a function of time directly from the dynamically generated chromoelectric field correlators.

We went beyond previous classical-statistical lattice calculations of  $\text{Im}[V_{\text{cl}}]$  by considering rather large lattice sizes and large values of  $\beta$  (small lattice spacings  $a$ ). We considered both  $SU(2)$  and  $SU(3)$  gauge groups and found that the potentials obtained obeyed a simple Casimir scaling. Using our CYM simulations on such lattices, we demonstrated that, for small values of quark-antiquark separation ( $r$ ), one can identify a continuum limit for  $\text{Im}[V_{\text{cl}}]$  if the lattice results are plotted as a function of  $m_D r$ . We also demonstrated that, in the region of small  $r$ , the lattice simulation results and perturbative lattice-regularized HCL results are very close to one another. At large  $r$ , we found that the lattice simulation results were only slightly different than the asymptotic value obtained using HCLs in the continuum limit ( $\beta \rightarrow \infty$ ). This indicates that the full non-perturbative result for  $\text{Im}[V_{\text{cl}}]$  is well-approximated by leading order lattice perturbation theory.

We also found that both our lattice simulation and HCL results were very well approximated by a functional form which can be obtained from a leading-order hard-thermal loop calculation. One only needs to take into account a different asymptotic value for  $r \rightarrow \infty$ , encoded in a parameter  $A_\infty$ , and a different scaling of the argument of the functional form, encoded in a parameter  $B$ . Using fits of this form and then expanding the result at small  $r$ , we were able to extract estimates for the heavy-quark diffusion coefficient  $\kappa$  from CYM lattice simulations, HTL, and HCL. The imaginary part of the potential was found to be

of the simple form  $V \simeq -\frac{1}{2}\kappa r^2$  at distances  $r \sim 1/T$  in all three approaches. We found that the HTL result for  $\kappa$  agreed to leading-logarithmic accuracy with direct calculations in continuum perturbation theory. Our results also demonstrated that  $\kappa$  obtained from the lattice simulation and HCL approaches were numerically similar, while both differing from the full leading-order quantum field theoretical result obtained using hard thermal loop resummations. Our analysis demonstrates as a proof of concept that one can extract the heavy-quark diffusion coefficient from the classical potential at low distances. We emphasize that the large lattice sizes and small lattice spacing used here were crucial to obtain these results.

Looking to the future, we plan to perform a similar calculation in an anisotropic plasma that is expanding along the longitudinal direction. This case is of phenomenological interest since the expansion of the quark-gluon plasma in relativistic heavy-ion collisions generates large momentum-space anisotropy. This renders the perturbative analytic calculation of the imaginary part of the heavy-quark potential ill-defined due to the presence of unstable modes in the soft gauge field propagator.

## ACKNOWLEDGMENTS

M.S. and B.K. were supported by the U.S. Department of Energy, Office of Science, Office of Nuclear Physics Award No. DE-SC0013470. We thank the Ohio Supercomputer Center for support under the auspices of Project No. PGS0253. The computational results presented have been also achieved in part using the Vienna Scientific Cluster (VSC).

## Appendix A: Tables

Our simulation results of  $\text{Im}[V_{\text{cl}}(r)]/g^2T$  for selected distances  $r/a$  and different parameters  $g^2T_0$  and the extracted temperatures  $g^2T$  are shown in Table I for  $a = 1$  and in Table II for  $a = 0.1$ .

---

[1] R. Averbeck, J. W. Harris, and B. Schenke, “Heavy-Ion Physics at the LHC,” in *The Large Hadron Collider: Harvest of Run 1*, edited by T. Schörner-Sadenius (2015) pp. 355–420.

		Im[V <sub>cl</sub> (r, t → ∞)]/g <sup>2</sup> T [a = 1]					
g <sup>2</sup> T <sub>0</sub>	g <sup>2</sup> T	r/a = 1	r/a = 2	r/a = 3	r/a = 4	r/a = 5	r/a = 6
0.20	0.185(2)	-0.030	-0.081(1)	-0.131(2)	-0.174(2)	-0.210(3)	-0.240(4)
0.25	0.227(4)	-0.037(1)	-0.099(2)	-0.158(3)	-0.209(4)	-0.252(5)	-0.288(6)
0.30	0.267(5)	-0.045(1)	-0.117(2)	-0.187(4)	-0.246(5)	-0.297(6)	-0.341(8)
0.35	0.306(7)	-0.052(1)	-0.136(3)	-0.217(5)	-0.286(7)	-0.345(8)	-0.397(10)
0.40	0.343(11)	-0.060(2)	-0.157(5)	-0.249(8)	-0.329(11)	-0.398(13)	-0.461(15)
0.45	0.379(11)	-0.069(2)	-0.179(5)	-0.284(8)	-0.376(11)	-0.457(14)	-0.529(16)
0.50	0.413(11)	-0.078(2)	-0.204(5)	-0.323(9)	-0.428(12)	-0.515(14)	-0.574(19)

TABLE I. Values of Im[V<sub>cl</sub>(r)]/g<sup>2</sup>T for different T<sub>0</sub> extracted from lattice simulations with a = 1, N = 64 and 224 configurations.

		Im[V <sub>cl</sub> (r, t → ∞)]/g <sup>2</sup> T [a = 0.1]					
g <sup>2</sup> T <sub>0</sub>	g <sup>2</sup> T	r/a = 10	r/a = 20	r/a = 30	r/a = 40	r/a = 50	r/a = 60
0.20	0.199(1)	-0.104(1)	-0.165(1)	-0.188(2)	-0.200(2)	-0.207(3)	-0.210(3)
0.25	0.248(2)	-0.114(1)	-0.171(1)	-0.191(2)	-0.200(2)	-0.207(2)	-0.212(3)
0.30	0.296(2)	-0.128(1)	-0.186(2)	-0.207(2)	-0.224(2)	-0.232(3)	-0.236(4)
0.35	0.345(3)	-0.137(1)	-0.197(2)	-0.218(2)	-0.229(2)	-0.243(3)	-0.258(4)
0.40	0.394	-0.146	-0.206(1)	-0.226(1)	-0.239(2)	-0.255(3)	-0.269(4)
0.45	0.442(3)	-0.152(1)	-0.209(2)	-0.225(2)	-0.235(3)	-0.248(3)	-0.255(4)
0.50	0.490(8)	-0.161(3)	-0.218(4)	-0.238(4)	-0.242(5)	-0.251(5)	-0.257(10)

TABLE II. Values of Im[V<sub>cl</sub>(r)]/g<sup>2</sup>T for different T<sub>0</sub> extracted from lattice simulations with a = 0.1, N = 252 (one configuration).

- [2] S. Acharya *et al.* (ALICE), (2020), [arXiv:2011.05758](https://arxiv.org/abs/2011.05758) [nucl-ex].
- [3] Songkyo Lee (ATLAS Collaboration), “Quarkonium production in Pb+Pb collisions with ATLAS,” Quark Matter 2020 <https://indico.cern.ch/event/792436/contributions/3535775/> (2017).
- [4] A. M. Sirunyan *et al.* (CMS), *Phys. Lett. B* **790**, 270 (2019), [arXiv:1805.09215](https://arxiv.org/abs/1805.09215) [hep-ex].

- [5] Z. Ye (STAR), *Proceedings, 8th International Conference on Hard and Electromagnetic Probes of High-energy Nuclear Collisions: Hard Probes 2016 (HP2016): Wuhan, Hubei, China, September 23-27, 2016*, Nucl. Part. Phys. Proc. **289-290**, 401 (2017), arXiv:1702.05651 [hep-ex].
- [6] Y. Akamatsu and A. Rothkopf, Phys. Rev. **D85**, 105011 (2012), arXiv:1110.1203 [hep-ph].
- [7] Y. Akamatsu, Phys. Rev. **D87**, 045016 (2013), arXiv:1209.5068 [hep-ph].
- [8] Y. Akamatsu, Phys. Rev. **D91**, 056002 (2015), arXiv:1403.5783 [hep-ph].
- [9] R. Katz and P. B. Gossiaux, Annals Phys. **368**, 267 (2016), arXiv:1504.08087 [quant-ph].
- [10] N. Brambilla, M. A. Escobedo, J. Soto, and A. Vairo, Phys. Rev. **D96**, 034021 (2017), arXiv:1612.07248 [hep-ph].
- [11] S. Kajimoto, Y. Akamatsu, M. Asakawa, and A. Rothkopf, Phys. Rev. **D97**, 014003 (2018), arXiv:1705.03365 [nucl-th].
- [12] N. Brambilla, M. A. Escobedo, J. Soto, and A. Vairo, Phys. Rev. **D97**, 074009 (2018), arXiv:1711.04515 [hep-ph].
- [13] J.-P. Blaizot and M. A. Escobedo, JHEP **06**, 034 (2018), arXiv:1711.10812 [hep-ph].
- [14] J.-P. Blaizot and M. A. Escobedo, Phys. Rev. **D98**, 074007 (2018), arXiv:1803.07996 [hep-ph].
- [15] X. Yao and T. Mehen, (2018), arXiv:1811.07027 [hep-ph].
- [16] O. Ålund, Y. Akamatsu, F. Laurén, T. Miura, J. Nordström, and A. Rothkopf, J. Comput. Phys. **425**, 109917 (2021), arXiv:2004.04406 [physics.comp-ph].
- [17] A. Islam and M. Strickland, Phys. Lett. B **811**, 135949 (2020), arXiv:2007.10211 [hep-ph].
- [18] A. Islam and M. Strickland, (2020), arXiv:2010.05457 [hep-ph].
- [19] N. Brambilla, M. A. Escobedo, M. Strickland, A. Vairo, P. Vander Griend, and J. H. Weber, (2020), arXiv:2012.01240 [hep-ph].
- [20] G. Lindblad, Communications in Mathematical Physics **48**, 119 (1976).
- [21] V. Gorini, A. Kossakowski, and E. C. G. Sudarshan, Journal of Mathematical Physics **17**, 821 (1976).
- [22] M. Laine, O. Philipsen, P. Romatschke, and M. Tassler, JHEP **03**, 054 (2007), arXiv:hep-ph/0611300 [hep-ph].
- [23] A. Dumitru, Y. Guo, and M. Strickland, Phys.Lett. **B662**, 37 (2008), arXiv:0711.4722 [hep-ph].

- [24] N. Brambilla, J. Ghiglieri, A. Vairo, and P. Petreczky, *Phys. Rev.* **D78**, 014017 (2008), [0804.0993 \[hep-ph\]](#).
- [25] Y. Burnier, M. Laine, and M. Vepsalainen, *Phys.Lett.* **B678**, 86 (2009), [arXiv:0903.3467 \[hep-ph\]](#).
- [26] A. Dumitru, Y. Guo, and M. Strickland, *Phys.Rev.* **D79**, 114003 (2009), [arXiv:0903.4703 \[hep-ph\]](#).
- [27] A. Dumitru, Y. Guo, A. Mocsy, and M. Strickland, *Phys.Rev.* **D79**, 054019 (2009), [arXiv:0901.1998 \[hep-ph\]](#).
- [28] M. Margotta, K. McCarty, C. McGahan, M. Strickland, and D. Yager-Elorriaga, *Phys.Rev.* **D83**, 105019 (2011), [arXiv:1101.4651 \[hep-ph\]](#).
- [29] Y. Guo, L. Dong, J. Pan, and M. R. Moldes, *Phys. Rev. D* **100**, 036011 (2019), [arXiv:1806.04376 \[hep-ph\]](#).
- [30] E. Eichten, K. Gottfried, T. Kinoshita, K. D. Lane, and T. M. Yan, *Phys. Rev. D* **21**, 203 (1980).
- [31] W. Lucha, F. F. Schoberl, and D. Gromes, *Phys. Rept.* **200**, 127 (1991).
- [32] N. Brambilla, A. Pineda, J. Soto, and A. Vairo, *Rev. Mod. Phys.* **77**, 1423 (2005), [arXiv:hep-ph/0410047 \[hep-ph\]](#).
- [33] N. Brambilla, J. Ghiglieri, P. Petreczky, and A. Vairo, *Phys. Rev.* **D82**, 074019 (2010), [arXiv:1007.5172 \[hep-ph\]](#).
- [34] A. Rothkopf, T. Hatsuda, and S. Sasaki, *Proceedings, 27th International Symposium on Lattice field theory (Lattice 2009): Beijing, P.R. China, July 26-31, 2009*, PoS **LAT2009**, 162 (2009), [arXiv:0910.2321 \[hep-lat\]](#).
- [35] A. Rothkopf, T. Hatsuda, and S. Sasaki, *Phys. Rev. Lett.* **108**, 162001 (2012), [arXiv:1108.1579 \[hep-lat\]](#).
- [36] Y. Burnier and A. Rothkopf, *Phys. Rev.* **D86**, 051503 (2012), [arXiv:1208.1899 \[hep-ph\]](#).
- [37] Y. Burnier and A. Rothkopf, *Phys. Rev. Lett.* **111**, 182003 (2013), [arXiv:1307.6106 \[hep-lat\]](#).
- [38] Y. Burnier and A. Rothkopf, *Phys. Lett.* **B753**, 232 (2016), [arXiv:1506.08684 \[hep-ph\]](#).
- [39] Y. Burnier, O. Kaczmarek, and A. Rothkopf, *JHEP* **12**, 101 (2015), [arXiv:1509.07366 \[hep-ph\]](#).
- [40] Y. Burnier and A. Rothkopf, *Phys. Rev.* **D95**, 054511 (2017), [arXiv:1607.04049 \[hep-lat\]](#).

- [41] Y. Burnier, O. Kaczmarek, and A. Rothkopf, *JHEP* **10**, 032 (2016), [arXiv:1606.06211 \[hep-ph\]](#).
- [42] D. Bala and S. Datta, *Phys. Rev. D* **101**, 034507 (2020), [arXiv:1909.10548 \[hep-lat\]](#).
- [43] D. Bala and S. Datta, *Phys. Rev. D* **103**, 014512 (2021), [arXiv:2009.00773 \[hep-lat\]](#).
- [44] M. Laine, O. Philipsen, and M. Tassler, *JHEP* **09**, 066 (2007), [arXiv:0707.2458 \[hep-lat\]](#).
- [45] A. Lehmann and A. Rothkopf, (2020), [arXiv:2012.10089 \[hep-lat\]](#).
- [46] D. Y. Grigoriev and V. A. Rubakov, *Nucl. Phys. B* **299**, 67 (1988).
- [47] J. Ambjorn, T. Askgaard, H. Porter, and M. Shaposhnikov, *Nucl.Phys.* **B353**, 346 (1991).
- [48] J. Ambjorn and A. Krasnitz, *Nucl. Phys. B* **506**, 387 (1997), [arXiv:hep-ph/9705380](#).
- [49] G. D. Moore, *Nucl. Phys. B* **480**, 657 (1996), [arXiv:hep-ph/9603384](#).
- [50] G. D. Moore and K. Rummukainen, *Phys. Rev. D* **61**, 105008 (2000), [arXiv:hep-ph/9906259](#).
- [51] A. Hart, M. Laine, and O. Philipsen, *Nucl. Phys. B* **586**, 443 (2000), [arXiv:hep-ph/0004060](#).
- [52] K. Kajantie, K. Rummukainen, and M. E. Shaposhnikov, *Nucl. Phys. B* **407**, 356 (1993), [arXiv:hep-ph/9305345](#).
- [53] J. Ambjorn and A. Krasnitz, *Phys. Lett. B* **362**, 97 (1995), [arXiv:hep-ph/9508202](#).
- [54] P. B. Arnold, D. Son, and L. G. Yaffe, *Phys. Rev. D* **55**, 6264 (1997), [arXiv:hep-ph/9609481](#).
- [55] J. Berges, K. Boguslavski, S. Schlichting, and R. Venugopalan, *JHEP* **05**, 054 (2014), [arXiv:1312.5216 \[hep-ph\]](#).
- [56] T. Epelbaum, F. Gelis, and B. Wu, *Phys. Rev. D* **90**, 065029 (2014), [arXiv:1402.0115 \[hep-ph\]](#).
- [57] J. Berges, K. Boguslavski, S. Schlichting, and R. Venugopalan, *Phys. Rev. D* **89**, 074011 (2014), [arXiv:1303.5650 \[hep-ph\]](#).
- [58] J. Berges, K. Boguslavski, S. Schlichting, and R. Venugopalan, *Phys. Rev. D* **89**, 114007 (2014), [arXiv:1311.3005 \[hep-ph\]](#).
- [59] S. Mrówczyński, *Phys. Lett.* **B393**, 26 (1997), [hep-ph/9606442](#).
- [60] P. Romatschke and M. Strickland, *Phys. Rev.* **D68**, 036004 (2003), [hep-ph/0304092](#).
- [61] P. B. Arnold, J. Lenaghan, and G. D. Moore, *JHEP* **0308**, 002 (2003), erratum added online, sep/29/2004, [arXiv:hep-ph/0307325 \[hep-ph\]](#).
- [62] M. Nopoush, Y. Guo, and M. Strickland, *JHEP* **09**, 063 (2017), [arXiv:1706.08091 \[hep-ph\]](#).
- [63] K. Boguslavski, A. Kurkela, T. Lappi, and J. Peuron, *Phys. Rev. D* **100**, 094022 (2019), [arXiv:1907.05892 \[hep-ph\]](#).
- [64] K. Boguslavski, A. Kurkela, T. Lappi, and J. Peuron, (2021), [arXiv:2101.02715 \[hep-ph\]](#).

- [65] K. Boguslavski, A. Kurkela, T. Lappi, and J. Peuron, *Phys. Rev. D* **98**, 014006 (2018), [arXiv:1804.01966 \[hep-ph\]](#).
- [66] A. Krasnitz, *Nucl. Phys. B* **455**, 320 (1995), [arXiv:hep-lat/9507025](#).
- [67] J. Smit and A. Tranberg, *JHEP* **12**, 020 (2002), [arXiv:hep-ph/0211243](#).
- [68] A. Kurkela and G. D. Moore, *Phys. Rev. D* **86**, 056008 (2012), [arXiv:1207.1663 \[hep-ph\]](#).
- [69] H. Matsuda, T. Kunihiro, B. Müller, A. Ohnishi, and T. T. Takahashi, *Phys. Rev. D* **102**, 114503 (2020), [arXiv:2007.06886 \[hep-ph\]](#).
- [70] G. Lepage, *J. Comput. Phys.* **27**, 192 (1978).
- [71] T. Hahn, *Comput. Phys. Commun.* **168**, 78 (2005), [arXiv:hep-ph/0404043](#).
- [72] G. D. Moore and D. Teaney, *Phys. Rev.* **C71**, 064904 (2005), [hep-ph/0412346](#).
- [73] S. Caron-Huot and G. D. Moore, *Phys. Rev. Lett.* **100**, 052301 (2008), [arXiv:0708.4232 \[hep-ph\]](#).
- [74] S. Caron-Huot and G. D. Moore, *JHEP* **02**, 081 (2008), [arXiv:0801.2173 \[hep-ph\]](#).
- [75] P. Petreczky and D. Teaney, *Phys. Rev.* **D73**, 014508 (2006), [arXiv:hep-ph/0507318 \[hep-ph\]](#).
- [76] H. B. Meyer, *New J. Phys.* **13**, 035008 (2011), [arXiv:1012.0234 \[hep-lat\]](#).
- [77] A. Francis, O. Kaczmarek, M. Laine, and J. Langelage, *Proceedings, 29th International Symposium on Lattice field theory (Lattice 2011): Squaw Valley, Lake Tahoe, USA, July 10-16, 2011*, *PoS LATTICE2011*, 202 (2011), [arXiv:1109.3941 \[hep-lat\]](#).
- [78] D. Banerjee, S. Datta, R. Gavai, and P. Majumdar, *Phys. Rev.* **D85**, 014510 (2012), [arXiv:1109.5738 \[hep-lat\]](#).
- [79] A. Francis, O. Kaczmarek, M. Laine, T. Neuhaus, and H. Ohno, *Phys. Rev.* **D92**, 116003 (2015), [arXiv:1508.04543 \[hep-lat\]](#).
- [80] N. Brambilla, V. Leino, P. Petreczky, and A. Vairo (TUMQCD), in *37th International Symposium on Lattice Field Theory (Lattice 2019) Wuhan, Hubei, China, June 16-22, 2019* (2019) [arXiv:1912.00689 \[hep-lat\]](#).
- [81] N. Brambilla, V. Leino, P. Petreczky, and A. Vairo, *Phys. Rev. D* **102**, 074503 (2020), [arXiv:2007.10078 \[hep-lat\]](#).
- [82] M. Laine, G. D. Moore, O. Philipsen, and M. Tassler, *JHEP* **05**, 014 (2009), [arXiv:0902.2856 \[hep-ph\]](#).
- [83] K. Boguslavski, A. Kurkela, T. Lappi, and J. Peuron, *JHEP* **09**, 077 (2020), [arXiv:2005.02418 \[hep-ph\]](#).

- [84] A. Ipp, D. I. Müller, and D. Schuh, *Phys. Rev. D* **102**, 074001 (2020), [arXiv:2001.10001](#) [[hep-ph](#)].
- [85] A. Ipp, D. I. Müller, and D. Schuh, *Phys. Lett. B* **810**, 135810 (2020), [arXiv:2009.14206](#) [[hep-ph](#)].